Contents lists available at ScienceDirect

Petroleum Science

journal homepage: www.keaipublishing.com/en/journals/petroleum-science



Original Paper

Numerical and experimental study on the falling film flow characteristics with the effect of co-current gas flow in hydrogen liquefaction process



Chong-Zheng Sun ^a, Yu-Xing Li ^b, Hui Han ^b, Xiao-Yi Geng ^b, Xiao Lu ^{a,*}

- ^a College of Energy Storage Technology, Shandong University of Science and Technology, Qingdao 266590, Shandong, China
- b College of Pipeline and Civil Engineering/Shandong Provincial Key Laboratory of Oil & Gas Storage and Transportation Safety, China University of Petroleum, Qingdao 266580, Shandong, China

ARTICLE INFO

Article history Received 28 April 2023 Received in revised form 12 October 2023 Accepted 6 November 2023 Available online 16 November 2023

Edited by Jie Hao and Meng-Jiao Zhou

Keywords: Hydrogen liquefaction Spiral wound heat exchanger Flow pattern transition Falling film flow

ABSTRACT

Liquid hydrogen storage and transportation is an effective method for large-scale transportation and utilization of hydrogen energy. Revealing the flow mechanism of cryogenic working fluid is the key to optimize heat exchanger structure and hydrogen liquefaction process (LH₂). The methods of cryogenic visualization experiment, theoretical analysis and numerical simulation are conducted to study the falling film flow characteristics with the effect of co-current gas flow in LH₂ spiral wound heat exchanger. The results show that the flow rate of mixed refrigerant has a great influence on liquid film spreading process, falling film flow pattern and heat transfer performance. The liquid film of LH₂ mixed refrigerant with column flow pattern can not uniformly and completely cover the tube wall surface. As liquid flow rate increases, the falling film flow pattern evolves into sheet-column flow and sheet flow, and liquid film completely covers the surface of tube wall. With the increase of shear effect of gas-phase mixed refrigerant in the same direction, the liquid film gradually becomes unstable, and the flow pattern eventually evolves into a mist flow.

© 2023 The Authors, Publishing services by Elsevier B.V. on behalf of KeAi Communications Co. Ltd. This is an open access article under the CC BY-NC-ND license (http://creativecommons.org/licenses/by-nc-nd/

4.0/).

1. Introduction

Due to the advantages of cleanness and high efficiency, hydrogen energy, as a representative of clean energy, will account for an increasing proportion in energy supply (Guo et al., 2022; Teng et al., 2023; Ding et al., 2022). Accelerating the layout of hydrogen energy industry is of great significance for promoting the transformation and upgrading of petroleum and petrochemical enterprises, and achieving the goal of carbon neutrality. Hydrogen storage and transportation are the key technology of hydrogen energy utilization. Compared with gaseous hydrogen, liquid hydrogen has the advantages of high hydrogen storage density per unit volume, high purity and high transportation efficiency (Xie et al., 2022; Son et al., 2022), which is convenient for large-scale hydrogen transportation and utilization (shown in Fig. 1).

The refrigeration cycle in hydrogen liquefaction process consists

Corresponding author. E-mail address: luxiao98@sdust.edu.cn (X. Lu).

of pre-cooling cycle and deep-cooling cycle (Sun et al., 2022). The deep-cooling cycle is mainly based on helium refrigeration. While, there are many kinds of refrigerants in the pre-cooling cycle. A mixed refrigerant hydrogen liquefaction system has been proposed by Krasae-in et al. (2011), which composes of neon, nitrogen, methane, ethane and butane. Compared with traditional refrigeration system, the mixed refrigerant refrigeration system has lower energy consumption. Sadaghiani and Mehrpooya (2017) proposed a new hydrogen liquefaction process with mixed refrigerant refrigeration, which has low energy consumption (4.41 kW h/kg LH₂, liquid hydrogen) and high efficiency (55.47%). The mixed refrigerant consists of 9 working fluids, including methane, ethane, propane, n-butane, n-pentane, hydrogen, nitrogen, R-14 and ethylene. A new integrated system combining biomass gasification and hydrogen liquefaction has been proposed by Ebrahimi et al. (2020). The mixed refrigerant in hydrogen liquefaction cycle is also composed of 9 working fluids, but it is slightly different from the mixed refrigerant proposed by Sadaghiani and Mehrpooya (2017). The mixed refrigerant in hydrogen liquefaction cycle proposed by Asadnia and Mehrpooya (2017) consists of 11

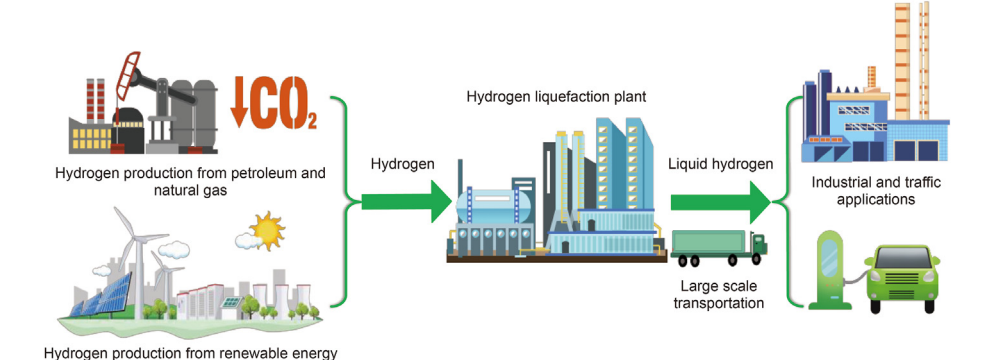


Fig. 1. Schematic diagram of production, transportation and utilization of liquid hydrogen.

components. A comprehensive exergy-based analysis is performed on a hydrogen liquefaction process of mixed refrigerant. The working medium of mixed refrigerant expanded from 5 components to 9 components (Ansarinasab et al., 2019). The results show that LH₂ heat exchangers play a chief role in exergy destruction cost

The structural optimization of main low-temperature heat exchanger is the key to improve the efficiency of liquefaction system (Sun et al., 2021, 2022a, 2022b). A numerical model of plain fin filled with catalyst has been established to study the influence of structural parameters of fin and catalyst layer on the LH₂ plate fin heat exchanger performance (Xu et al., 2022a, 2022b). Skaugen et al. (2020) have constructed mathematical models for catalystfilled heat exchanger and compared the performances of LH₂ spiral wound and plate fin heat exchanger. The results show that SWHE (spiral wound heat exchanger) has a lower exergy destruction in large-scale hydrogen liquefaction process. Falling film evaporation is the dominant heat transfer technology of LH2 spiral wound heat exchanger. Wang et al. (2008) studied the type of flow pattern between two adjacent tubes and He et al. (2007) analyzed the effects of Reynolds number, spray type and tube spacing on flow pattern transition. Chen et al. (2015), Li et al. (2017) and Shen et al. (2015) studied the heat and mass transfer characteristics of falling-film evaporator. The influence factors of tube diameter, tube spacing, flow rate and fluid properties on flow pattern have been experimentally studied by Chung et al. (2012), Wang and Jacobi (2014). Mitrovic (2005) found that column flow pattern was the most stable among 5 type flow through experimental method. Sun et al. (2023) experimentally and numerically studied the falling film flow process on the outer wall. Yu et al. (2023) investigated the experimental and theoretical methods for film thickness and interface fluctuations in falling film flow process. Bohra et al. (2019) studied droplet characteristics and flow state transition in horizontal-tube falling-film absorbers. Wang et al. (2019) and Chen et al. (2022) studied the film thickness distribution of horizontal tube falling film with column flow, droplet and sheet flow. Lin et al. (2019) analyzed the spatial distribution of liquid film thickness through the 3D visualization method. Liu et al. (2019) experimentally studied the droplet flow of falling film pattern between tubes.

The composition of mixed refrigerant in hydrogen liquefaction process is more complex than that of natural gas liquefaction process. There will be a longer gas-liquid two-phase coexistence zone in the flow and heat transfer process of LH₂ mixed refrigerant. Numerical simulation of falling film flow shows that two-phase flow has various flow patterns, and the flow pattern varies with different flow rate (Chen et al., 2015). Based on the adaptive-grid Eulerian method, Havestini and Ormiston (2022) built a numerical model to capture the gas-liquid two-phase interface. Qi et al.

(2021) constructed a theoretical model to study the break-up characteristics of gas-liquid two-phase falling film convective absorption, which provides a theoretical explanation for falling film rupture. A numerical model and a visualization experiment system are built to study the performance of counter-current gas-liquid falling film flow, which provides a theoretical basis for the design and optimization of heat exchanger (Zhang et al., 2022). Zhou et al. (2023) built a two-dimensional model to study the effect of cocurrent gas flow on the falling film flow hydrodynamic characteristics. Eskin (2022) built an engineering model of a turbulent falling liquid film with gas flow to study momentum and heat transfer across the liquid film. Kofman et al. (2017) experimentally studied the falling water film sheared by a counter-current air flow. The falling film thickness and wave velocity are measured through visual experimental device to study the effect of counter-current gas flow on water waves.

The ideal state of refrigerant falling film flow in LH2 spiral wound heat exchanger is that a thin liquid film is evenly spread on the tube surface, providing cooling capacity for the condensation process of feed hydrogen gas in the tube. The spreading behavior of liquid film is influenced by the mass flow rate of mixed refrigerant. Compared to the natural gas liquefaction process using mixed refrigerants, the composition of mixed refrigerants in the hydrogen liquefaction process is more complex. Complex non-azeotropic refrigerants have different component migration characteristics, and two-phase flow area is longer. The gas-phase flow has a greater impact on the liquid-phase falling film flow. At present, a limited number of researches are available on the falling film flow and heat transfer performance of LH₂ spiral wound heat exchanger. Furthermore, the lack of investigation on falling film flow characteristics with the effect of co-current gas flow has limited the design and optimization of LH2 SWHE. Therefore, the purpose of this paper is to investigate falling film flow characteristics with the effect of co-current gas flow based on cryogenic experimental device, visualization experimental device and numerical simulation model.

2. Numerical and experimental research methods

A numerical simulation model of falling film flow with the effect of co-current gas flow has been established to quantitatively obtain the parameters such as liquid film thickness and velocity.

The continuity equation of three-dimensional (3D) numerical model is as follows:

$$\nabla \cdot \overrightarrow{u} = \frac{\partial u_x}{\partial x} + \frac{\partial u_y}{\partial y} + \frac{\partial u_z}{\partial z} = 0 \tag{1}$$

The momentum equation is as follows:

$$\rho\left(\frac{\partial u_X}{\partial t} + u_X \frac{\partial u_X}{\partial x} + u_Y \frac{\partial u_X}{\partial y} + u_Z \frac{\partial u_X}{\partial z}\right) = -\frac{\partial p}{\partial x} + \mu\left(\frac{\partial^2 u_X}{\partial x^2} + \frac{\partial^2 u_X}{\partial y^2} + \frac{\partial^2 u_X}{\partial z^2}\right)$$
+ F_X

(2)

$$\rho\left(\frac{\partial u_y}{\partial t} + u_x \frac{\partial u_y}{\partial x} + u_y \frac{\partial u_y}{\partial y} + u_z \frac{\partial u_y}{\partial z}\right) = -\frac{\partial p}{\partial y} + \mu\left(\frac{\partial^2 u_y}{\partial x^2} + \frac{\partial^2 u_y}{\partial y^2} + \frac{\partial^2 u_y}{\partial z^2}\right) + F_V$$

(3)

$$\rho\left(\frac{\partial u_z}{\partial t} + u_x \frac{\partial u_z}{\partial x} + u_y \frac{\partial u_z}{\partial y} + u_z \frac{\partial u_z}{\partial z}\right) = -\frac{\partial p}{\partial z} + \mu\left(\frac{\partial^2 u_z}{\partial x^2} + \frac{\partial^2 u_z}{\partial y^2} + \frac{\partial^2 u_z}{\partial z^2}\right) + F_z$$
(4)

The momentum source term is as follows:

$$\overrightarrow{F} = F_{x} \overrightarrow{i} + F_{y} \overrightarrow{j} + F_{z} \overrightarrow{k}$$
 (5)

 \vec{F} is the momentum source term, which includes gravity and surface tension. With gas-liquid phase shear, gas-liquid drag force should be considered:

$$\overrightarrow{F} = \overrightarrow{F_G} + \overrightarrow{F_G} + \overrightarrow{F_{IG}} \tag{6}$$

The gravity source term $\overrightarrow{F_G}$ is as follows:

$$\overrightarrow{F_{\mathsf{G}}} = \rho \overrightarrow{g} \tag{7}$$

The surface tension source term $\overrightarrow{F_{\sigma}}$ can be calculated through the continuous surface force (CSF) model proposed by Brackbill et al. (1992) and given in Eq. (8). The surface tension effect is achieved by adding a momentum source term to the momentum equation.

$$\overrightarrow{F_{\sigma}} = \sigma \frac{\rho \kappa \nabla \alpha}{0.5(\rho_{\rm G} + \rho_{\rm L})} \tag{8}$$

where, κ represents the surface tension curvature, and the calculation expression is as follows:

$$\kappa = -\nabla \cdot \overrightarrow{n} \tag{9}$$

where, the normal vector of the unit surface \overrightarrow{n} is:

$$\overrightarrow{n} = \overrightarrow{n}\cos\psi + \overrightarrow{n}\sin\psi \tag{10}$$

where, ψ is the static contact angle.

Static contact angle is commonly used to measure the macroscopic wettability of solid surfaces, and is the key to understanding the interaction between liquid and solid at the two-phase interface. The apparent contact angle of droplets attached to a solid surface in equilibrium can be described by the classical Young's equation.

$$\gamma_{\rm sv} - \gamma_{\rm sl} = \gamma_{\rm lv} \cos \psi \tag{11}$$

where, γ_{sv} , γ_{sl} and γ_{lv} represent the solid-gas, solid-liquid and gasliquid interfacial tension, respectively.

The gas-liquid drag force model (Li et al., 2016):

$$\overrightarrow{F_{LG}} = \frac{1}{2} \frac{\rho_{G} f_{LG} \left| \overrightarrow{u}_{L} - \overrightarrow{u}_{G} \right| \left(\overrightarrow{u}_{L} - \overrightarrow{u}_{G} \right)}{\delta}$$
(12)

where, f_{IG} is the gas-liquid interface friction coefficient:

$$f_{\rm LG} = f_{\rm SC} \left[1 + 24 \left(\frac{\rho_{\rm L}}{\rho_{\rm G}} \right)^{1/3} \frac{\delta}{d} \right] \tag{13}$$

when Re < 2000,

$$f_{SC} = \frac{16}{Re} \tag{14}$$

when Re > 2000,

$$\frac{1}{\sqrt{f_{SC}}} = 3.48 - 4\lg\left(\frac{2\varsigma}{d} + \frac{9.35}{\text{Re}\sqrt{f_{SC}}}\right)$$
 (15)

where, δ is the liquid film thickness, $\rho_{\rm L}$ is the liquid-phase density, $\rho_{\rm G}$ is the gas-phase density, d is the tube diameter, ς is the roughness, Re is the Reynolds number.

Due to the strong shear effect of co-current gas flow, a turbulence model is selected in the numerical simulation model. The standard k- ε is the most widely used model, with moderate computational complexity, significant data accumulation, and considerable accuracy. Therefore, the standard k- ε model is suitable for simulating the flow process of completely turbulent fluids and can effectively solve practical engineering problems. The equations of standard k- ε model are:

$$\frac{\partial}{\partial t}(\rho k) + \frac{\partial}{\partial x_i}(\rho k \mu_i) = \frac{\partial}{\partial x_j} \left[\left(\mu + \frac{\mu_t}{\sigma_k} \right) \frac{\partial k}{\partial x_j} \right] + G_k + G_b - \rho_{\varepsilon} - Y_M + S_k$$
(16)

$$\frac{\partial}{\partial t}(\rho\varepsilon) + \frac{\partial}{\partial x_i}(\rho\varepsilon u_i) = \frac{\partial}{\partial x_j} \left[\left(\mu + \frac{\mu_t}{\sigma_\varepsilon} \right) \frac{\partial \varepsilon}{\partial x_j} \right] + N_{1\varepsilon} \frac{\varepsilon}{k} (G_k + N_{3\varepsilon} G_b)
- N_{2\varepsilon} \rho \frac{\varepsilon^2}{k} + S_{\varepsilon}$$
(17)

where, k is the turbulent kinetic energy; ε is the kinetic energy dissipation rate; G_k is the turbulent flow energy term generated by the time averaged velocity gradient; G_b is the turbulent flow energy term generated by buoyancy; S_k and S_ε are the custom source items for S_ε and S_ε are the Turbulent Prandtl number; S_ε are dimensionless number.

The coupled VOF and Level Set method has been proposed by Sussman and Puckett (2000). In the coupled VOF and Level Set method, the good physical conservation of VOF method and the advantages of Level Set method in solving interface geometric parameters are combined to better capture the two-phase free interface. Therefore, the coupled VOF and Level Set method is used to simulate the falling film flow in this paper. γ represents the volume fraction of a certain phase in a grid. The main equation of the model is as follows:

$$\frac{\partial \gamma_{g}}{\partial t} + \nabla \cdot \left(\gamma_{g} \overrightarrow{u} \right) = 0 \tag{18}$$

where, γ_g represents the gas-phase volume fraction, and γ_l = 1- γ_g is the liquid-phase volume fraction. Discretization of momentum

equations is based on QUICK (Quadratic upstream interpolation for convective kinematics) scheme. The inlet boundary condition is the mass flow inlet boundary. The left and right boundary conditions are symmetry boundary.

Due to the small pressure gradient in the fluid domain, it is assumed that the physical properties of the test medium are constant. The working medium is assumed as the incompressible fluid. The density of gas-phase working medium is 7.09 kg/m³, the density of liquid-phase working medium is 855.4 kg/m³, and the surface tension is 0.3367 N/m. The hydrogen liquefaction process is divided into pre-cooling cycle and deep-cooling cycle. The deepcooling cycle mainly consists of helium expansion refrigeration, while the pre-cooling cycle mainly consists of complex mixed refrigerants with a temperature range of 25 to -190 °C. The testing temperature range is the temperature range of complex mixed refrigerants in the hydrogen liquefaction process. The grid of threedimensional (3D) numerical model is shown in Fig. 2. The thickness of the first mesh near the wall is 0.010 mm, which can capture the gas-liquid interface accurately. The length and width of the upper inlet and lower outlet are 24 mm and 20 mm, respectively. The length of liquid-phase inlet is 4 mm. The outer diameter of test tube D is 12 mm, and tube spacing S is 4 mm. The time step is 1×10^{-6} s. To confirm the mesh-independent of numerical results, the simulation model with 1385207, 2557379 and 3789557 grids are conducted. When the grid number changes from 2557379 to 3789557, the average change of liquid film thickness is 1.18%. The numerical results indicate that 2557379 grid is sufficient to provide reasonable mesh-independent results.

The cryogenic heat transfer and visualization experimental device of falling film flow in spiral wound heat exchanger has been built and shown in Fig. 3. The experimental device is divided into a visual test system and a cryogenic heat transfer test system. Both experimental systems can achieve long-term stable operation. The high-speed camera, central control image acquisition system and LED light are installed in the visualization experimental system of spiral wound heat exchanger. The gas-liquid interface is recorded in

real time to provide experimental support for numerical simulation results and study the flow pattern evolution of falling film flow (shown in Fig. 4). The falling film flow and heat transfer test system can maintain cryogenic environment through cold box, compressor and low temperature throttle valve. During the cryogenic experiment, electrical energy is converted into pressure energy through a compressor. Then, pressure energy is converted into cold energy through a low temperature throttle valve. The heat exchange between mixed refrigerant and feed gas is carried out through the cold box. The cold energy is transferred to feed gas by mixed refrigerant. Based on the central control data acquisition system, the influence of refrigerant and feed gas flow rates on falling film flow and heat transfer characteristics has been studied. The uncertainty of pressure transmitter (MPa) is $\pm 0.075\%$. The uncertainty of mass flow meter (kg/h) is $\pm 0.35\%$. The uncertainty of temperature is ± 0.1 °C. As shown in Fig. 4, by qualitatively comparing the experimental and numerical simulation results (D = 12 mm, S = 4 mm, Re = 510, P = 100 kPa, t = 315 ms), the numerical simulation of falling film flow pattern is consistent with the experiment.

From Fig. 5, compared with the correlation equation proposed by Hou et al. (Eq. (19)) (2012) for predicting liquid film thickness, the average error is 3.362%. While, the relative error between theoretical model and numerical simulation model is larger than 20% for circumferential angles from 100° to 150°. This is because the calculation relationship proposed by Hou et al. (2012) is improved by Nusselt (1916), which proposed the integral method to calculate the liquid film thickness along the tube wall, assuming that the falling film flow is laminar. The studied media is water or seawater. The calculation formula can well explain and express the distribution trend of the liquid film along the circumferential angle. In the actual visualization experiment process, this paper found that due to the absence of tube outer wall constraints, the liquid film is in a quasi-static equilibrium state, and there will be significant fluctuations in the liquid film locally. The falling film flow of refrigerant is not laminar. Therefore, the Hou model (Hou et al.,

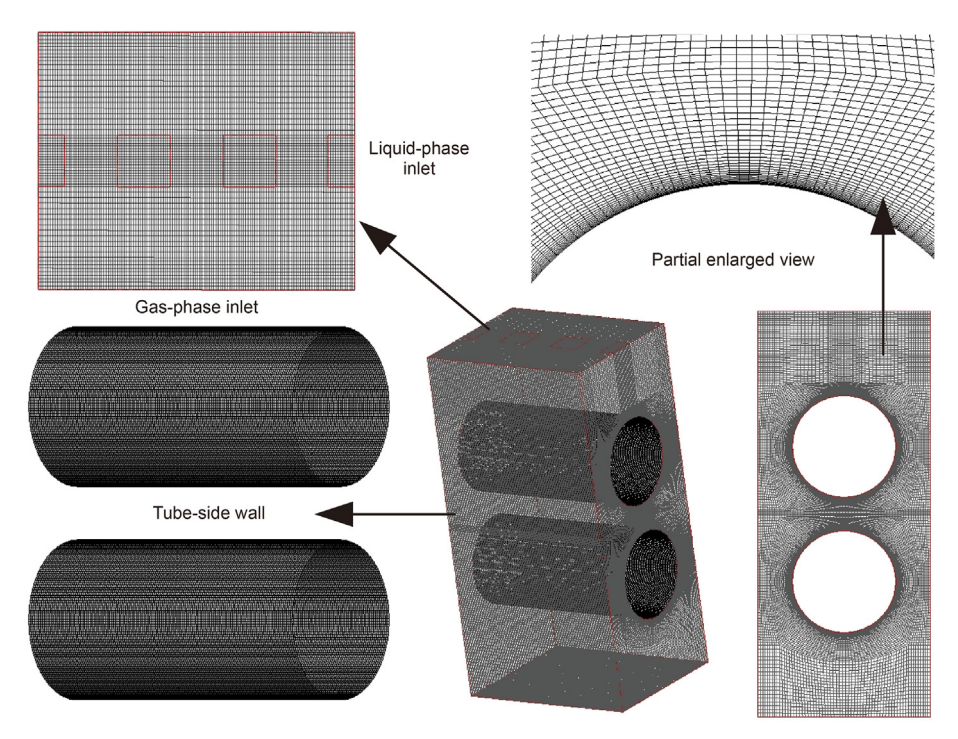


Fig. 2. The overall meshing and partial enlarged view of falling film flow.

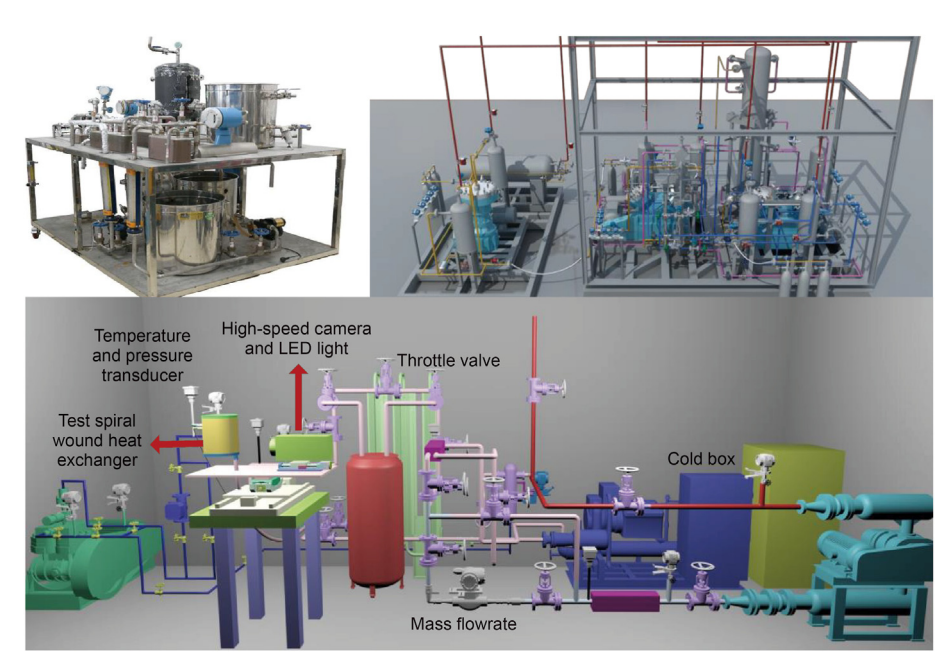


Fig. 3. Cryogenic heat transfer and visualization experimental device of falling film flow.

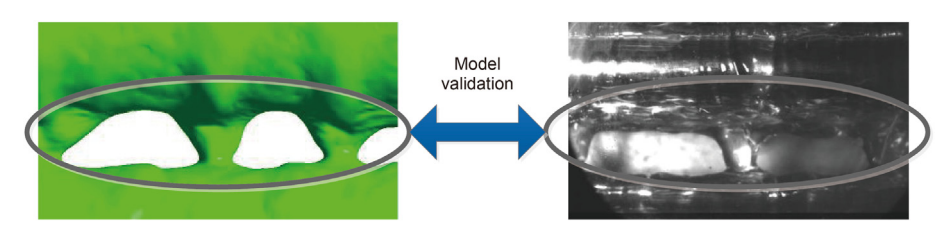


Fig. 4. The comparison between experimental and numerical results.

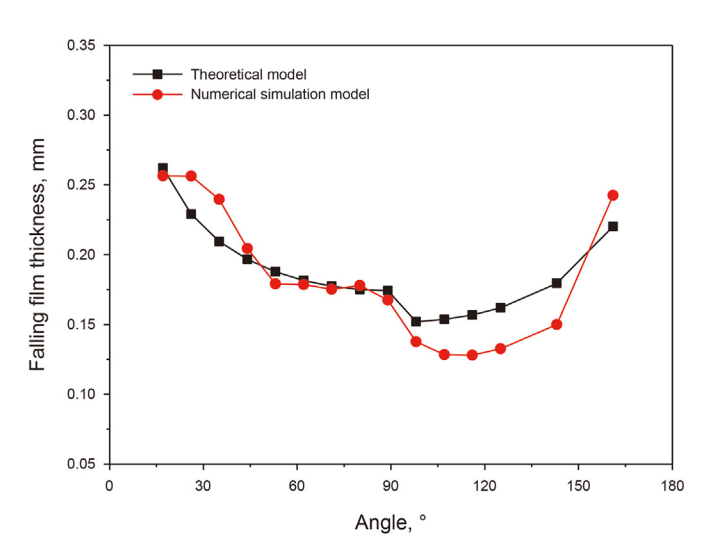


Fig. 5. The comparison between theoretical and numerical simulation model.

2012) is accurate in predicting the average liquid film thickness and the distribution trend of liquid film. From Fig. 5, the variation trend of liquid film thickness with circumferential angle is similar between the theoretical model and the numerical simulation model. In addition, quantitative comparison of numerical simulation results with experimental results is given in Table 1. It can be seen

that the maximum and average deviations between experimental results and simulation results are -12.188% and -1.779%, respectively. Therefore, the numerical simulation model is accurate enough to describe the falling film flow :

$$\delta = c \left(\frac{S}{d}\right)^n \left(\frac{3\mu\Gamma}{\rho_L(\rho_L - \rho_G)g\sin\alpha}\right)^{1/3} \tag{19}$$

where, S is the tube spacing, d is the tube diameter; ρ_G and ρ_L are the gas-phase and liquid-phase density; c and n are constants; α is the circumferential angle; Γ is the liquid mass flow rate per unit pipe length; μ is the dynamic viscosity.

3. Results and discussion

3.1. Falling film flow characteristics of liquid-phase refrigerant

The ideal state of refrigerant falling film flow in LH₂ spiral wound heat exchanger is that the thin liquid film is evenly spread on the tube surface, providing cooling capacity for the condensation process of hydrogen gas. The spreading behavior of the liquid film is influenced by the mass flow rate of mixed refrigerant. Therefore, the falling film flow characteristics and velocity distribution of LH₂ mixed refrigerant with different flow rates are studied and shown in Fig. 6. It can be seen that when the mass flow rate m_L is 7.2 kg/h, the flow rate is relatively small. With the function of top liquid distributor, the LH₂ mixed refrigerant is evenly dropped, and liquid film has good spreading ability at the first tube.

Table 1Ouantitative comparison of numerical simulation results with experimental results.

	Numerical simulation results, mm	Experimental results, mm	Deviation, %
The narrowest thickness at the bottom of liquid column	2.156	2.039	5.410
Thickness in the middle of liquid column	3.016	2.997	0.645
Thickness of the top of liquid column	5.308	5.101	3.905
The thickest liquid film outside the bottom tube	0.640	0.673	-5.049
Thinnest liquid film outside the bottom tube	0.212	0.219	-3.397
Inlet liquid column width	1.517	1.702	-12.188
Falling film flow pattern	Column flow pattern	Column flow pattern	

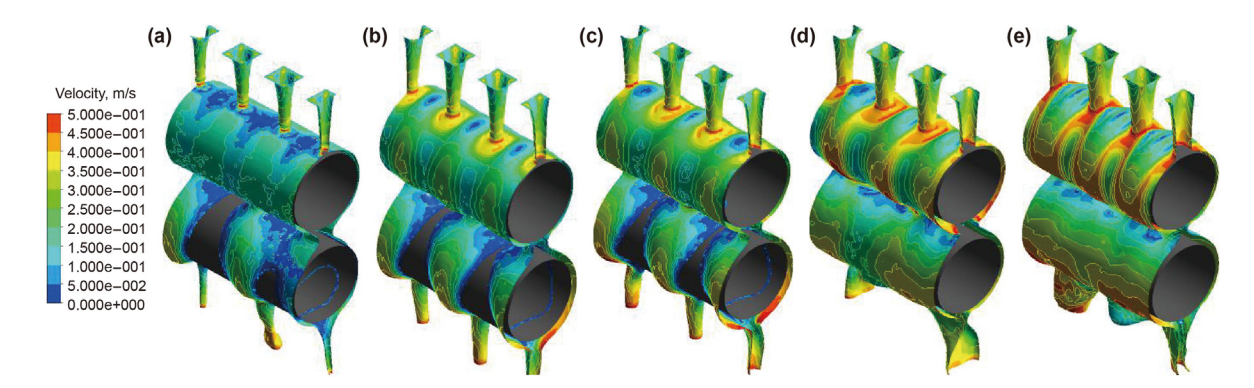


Fig. 6. The falling film flow characteristics and velocity distribution of LH₂ mixed refrigerant with different flow rates: (a) 7.2 kg/h, (b) 10.8 kg/h, (c) 14.4 kg/h, (d) 21.6 kg/h, (e) 28.8 kg/h.

When the liquid film converges between tubes, a narrow and wide liquid column is formed. The liquid column spreads outside the second tube, presenting a column flow pattern. Due to the complex composition of LH₂ mixed refrigerant, the radial flow rate is much greater than the axial flow rate, resulting in a large number of dry areas outside the tube.

When the mass flow rates increase to 10.8 kg/h and 14.4 kg/h (Fig. 6(b) and (c)), the liquid vertically descends in the form of a liquid column from the inlet, and the top liquid column widens. After contacting with the first tube, the liquid quickly spreads along the axial and circumferential directions. Between two liquid columns, the peak area is formed due to the interaction of liquid films on both sides. The falling film flow pattern exhibits a column flow pattern, with a narrow upper and wide lower liquid column. Although the flow pattern between tubes is stable, a large number of dry areas appear on the second tube wall. This is because the radial flow rate of LH2 mixed refrigerant is greater than axial flow rate, resulting in a large number of dry areas with column flow pattern. The falling film dry patch distribution of the second tube is calculated and given in Fig. 7. When the circumferential angle is in the range from 0° to 140° , the range of dry patch increases. When the circumferential angle is greater than 140°, the scope of dry area gradually shrinks.

As shown in Fig. 6(d), when the mass flow rate is 21.6 kg/h, the top liquid column significantly thickens. The liquid film outside the first tube is similar to the lower mass flow rate ($m_{\rm L}=7.2$ kg/h, 10.8 kg/h and 14.4 kg/h), with obvious peak zone and trough zone. The flow pattern between the tubes presents a relatively unstable sheet-column flow pattern, with a column flow pattern on the left and a sheet flow pattern on the right. Due to the wide landing point of liquid sheet, the second tube surface is completely covered with liquid film. The liquid film presents a ripple shape. When the mass flow rate increases to 28.8 kg/h, the liquid film on the first tube surface is relatively stable, and the flow rate further increases. The flow pattern presents a stable sheet flow pattern, with liquid fans connected into sheets and continuous landing points, resulting in

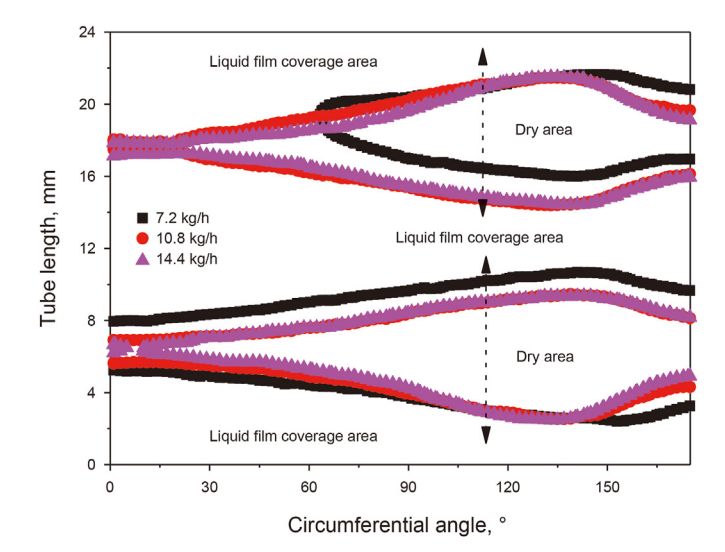
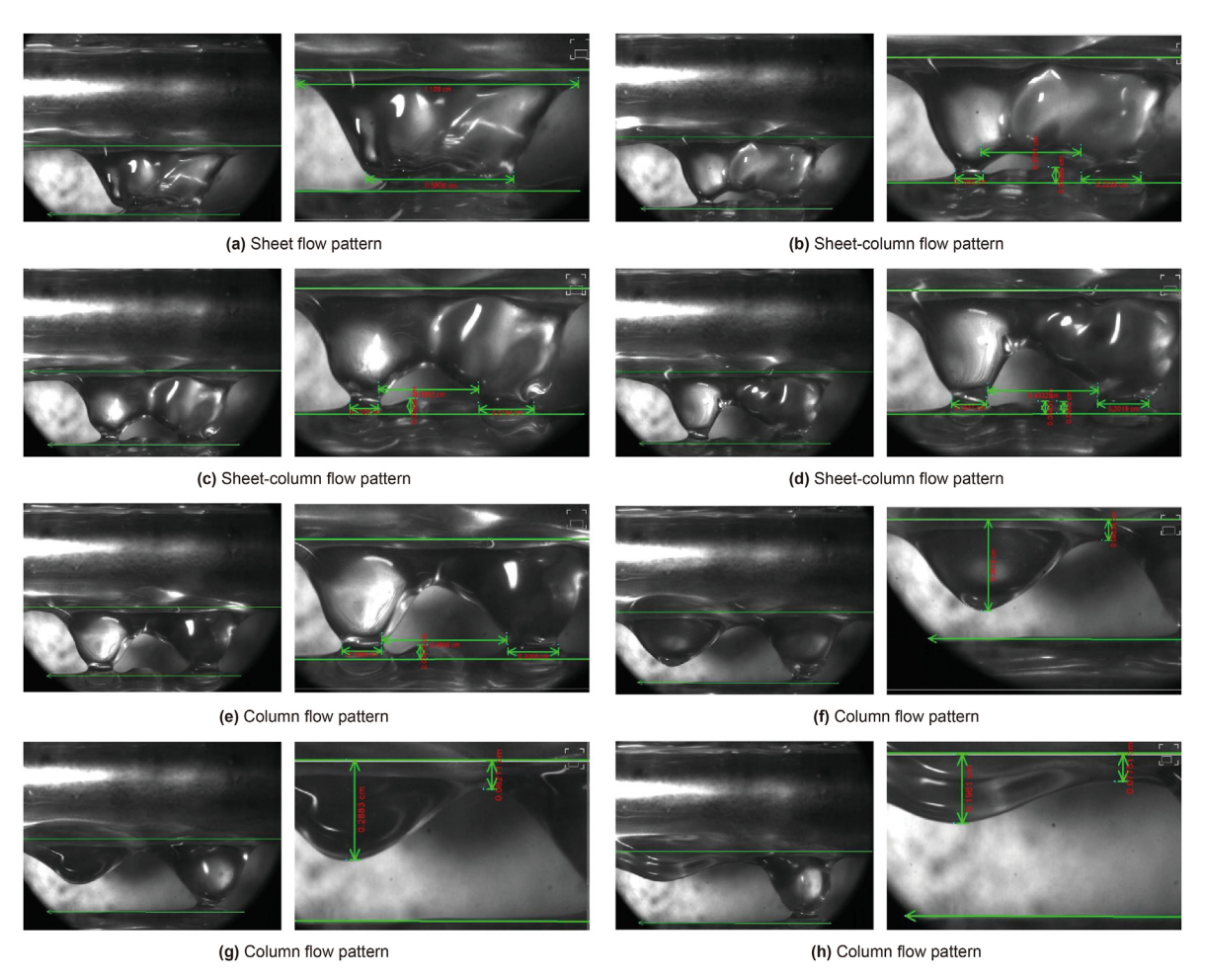


Fig. 7. The falling film dry patch distribution of the second tube.

better spreading of liquid film outside the second tube.

The test spiral wound heat exchanger and high-speed camera are constructed to experimentally study the evolution process of falling film flow pattern. The liquid distribution of falling film flow is shown in Fig. 8, which microscopically describes the evolution process from sheet flow pattern to column flow pattern. The right image of Fig. 8 is an enlargement of the left image, and gives quantitative local parameters.

As shown in Fig. 8(a), the falling film flow pattern is stable sheet flow pattern at the beginning. The upper part of the liquid sheet is wider (1.109 cm), while the lower part is narrower (0.5306 cm). From Fig. 8(b), with the decrease of flow rate, the liquid sheet starts to break from the bottom and split to form a liquid column. The liquid column continuously splits and separates, and finally forms



 $\textbf{Fig. 8.} \ \ \textbf{The liquid distribution of falling film flow process}.$

two liquid columns (shown in Fig. 8(c)-(e)). The lateral distance of liquid column is 0.4946 cm. Finally, as the flow rate continues to decrease, the liquid column on one side is stable. On the other side, the liquid column gradually contracts, and finally forms a liquid belly (shown in Fig. 8(f)-(h)). The liquid belly width is 0.1961 cm.

Fig. 9 quantitatively gives the falling film flow thickness distribution with different mass flow rates ($m_{\rm L}$) of liquid-phase mixed refrigerant outside the first tube. It can be seen that when $m_{\rm L}=21.6$ kg/h, the falling film flow pattern evolves from sheet flow pattern to column flow pattern. The sheet-column flow pattern is extremely unstable. The fluctuation between the peak and trough of liquid film is large. Some wave peaks are even higher than the sheet flow pattern ($m_{\rm L}=28.8$ kg/h). When $m_{\rm L}=7.2$ kg/h, the liquid film spreads evenly without large peaks and troughs. When the flow rate is greater than 7.2 kg/h, the wave peak of liquid film thickness appears along the axial direction. The thickness distribution of liquid film is relatively regular with small circumference angle. When the circumference angle is greater than 80°, the stability of liquid film is poor. At the same circumferential position, the flow rate has a great influence on liquid film thickness distribution.

When the circumferential angle is 20° , with $m_L=10.8$ kg/h, 14.4 kg/h and 28.8 kg/h, the maximum liquid film thicknesses are 0.77 mm, 0.89 mm and 1.31 mm, respectively. The minimum liquid film thicknesses are 0.31 mm, 0.34 mm and 0.43 mm, and velocities are 0.33 m/s, 0.41 m/s and 0.46 m/s, respectively. When the circumferential angle is 100° , the maximum liquid film thicknesses are 0.53 mm, 0.57 mm and 0.78 mm, respectively. The minimum

liquid film thicknesses are 0.37 mm, 0.39 mm and 0.48 mm, and velocities are 0.12 m/s, 0.14 m/s and 0.28 m/s, respectively. When the circumferential angles are 20°, 60°, 100° and 140°, with $m_{\rm L}=28.8$ kg/h, the maximum liquid film thicknesses are 1.31 mm, 0.96 mm, 0.78 mm and 0.91 mm, and velocities are 0.14 m/s, 0.31 m/s, 0.41 m/s and 0.45 m/s, respectively.

3.2. The influence of the co-current gas flow on falling film flow characteristics

The falling film flow characteristics and velocity distribution with $m_{\rm G}=3.6~{\rm kg/h}~(\nu_{\rm G}=0.508~{\rm m}^3/{\rm h}),~m_{\rm L}=21.6~{\rm kg/h}~(\nu_{\rm L}=0.025~{\rm m}^3/{\rm h})$ and 28.8 kg/h ($\nu_{\rm L}=0.034~{\rm m}^3/{\rm h}$) are shown in Figs. 10 and 11. It can be seen that due to the small flow rate of gas phase $m_{\rm G}=3.6~{\rm kg/h}~(\nu_{\rm G}=0.508~{\rm m}^3/{\rm h})$, the co-current gas flow has little effect on falling film flow pattern and velocity distribution. Moreover, as time goes by, the shape of liquid film and flow pattern remains stable. When the liquid phase flow rate $m_{\rm L}$ increases to 28.8 kg/h ($\nu_{\rm L}=0.034~{\rm m}^3/{\rm h}$), the falling film flow characteristics and velocity distribution are shown in Fig. 11. Similar to $m_{\rm L}=21.6~{\rm kg/h}~(\nu_{\rm L}=0.025~{\rm m}^3/{\rm h})$, the co-current gas flow has little effect on the falling film flow pattern and velocity distribution, and the inter tube flow pattern is a completely sheet flow.

The wavy film flow characteristics and velocity distribution with $m_G=18$ kg/h ($v_G=2.539$ m 3 /h), $m_L=21.6$ kg/h ($v_L=0.025$ m 3 /h) and 28.8 kg/h ($v_L=0.034$ m 3 /h) are shown in Figs. 12 and 13. It can be seen that the co-current gas flow increases the flow rate of liquid

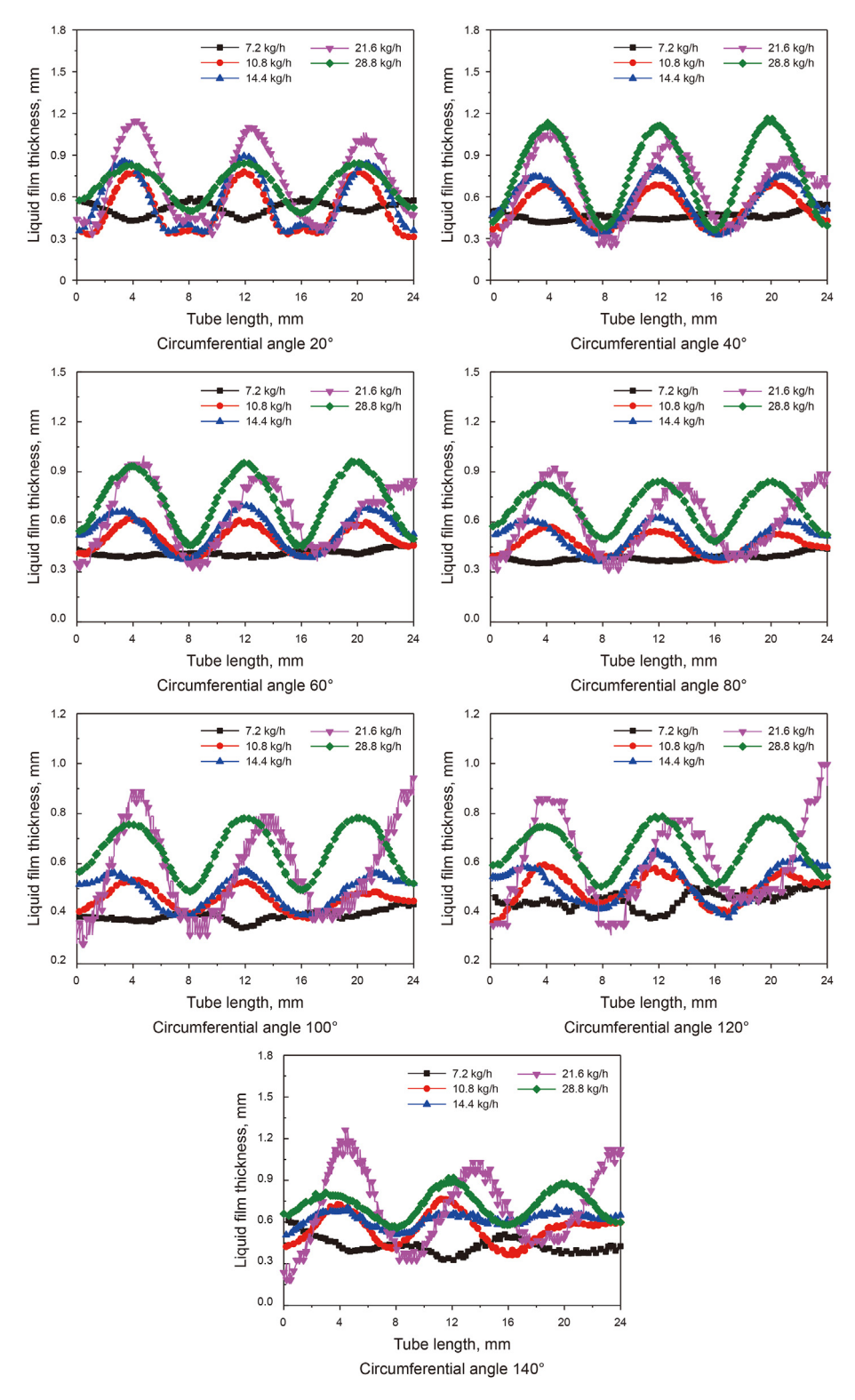


Fig. 9. The falling film flow thickness distribution with different mass flow rates of liquid-phase mixed refrigerant outside the first tube.

film descent, and the flow pattern of LH $_2$ mixed refrigerant evolves from falling film flow pattern (sheet flow pattern and sheet-column flow pattern) to wavy flow pattern. As shown in Fig. 12, the shear effect of co-current gas flow disrupts the stability of sheet-column flow pattern. The liquid film on upper part of the tube is sheared thin by the shear effect, and the liquid film on lower part of the tube

gradually accumulates with the push of gas flow. When the liquid-phase mass flow rate of LH $_2$ mixed refrigerant increases to 28.8 kg/h, the falling film flow characteristics and its velocity over time are shown in Fig. 13. At 25.894 ms, the co-current gas flow has not yet affected the liquid film spreading process, and the uniformity of liquid film spreading is good. At 53.889 ms, the shear effect of co-

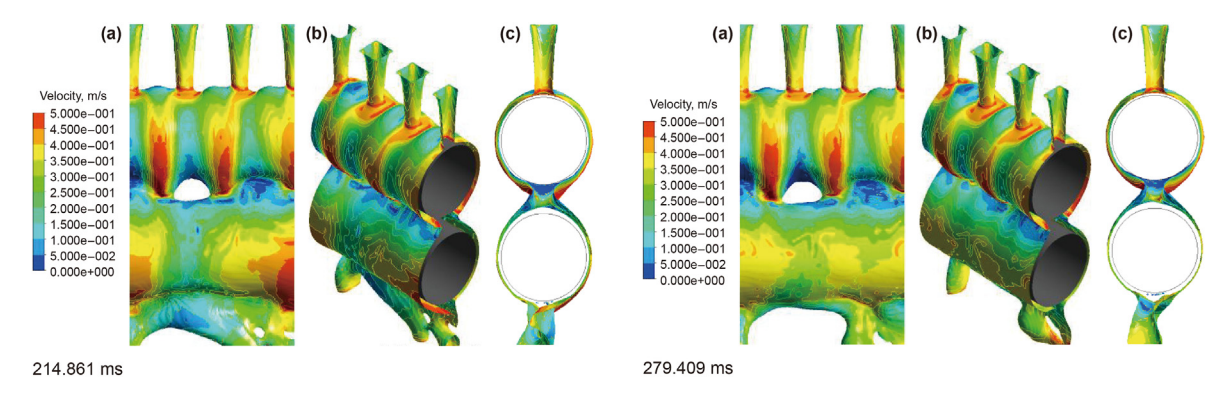


Fig. 10. The falling film flow characteristics and velocity distribution of LH₂ mixed refrigerant with $m_G = 3.6$ kg/h ($v_G = 0.508$ m³/h), $m_L = 21.6$ kg/h ($v_L = 0.025$ m³/h).

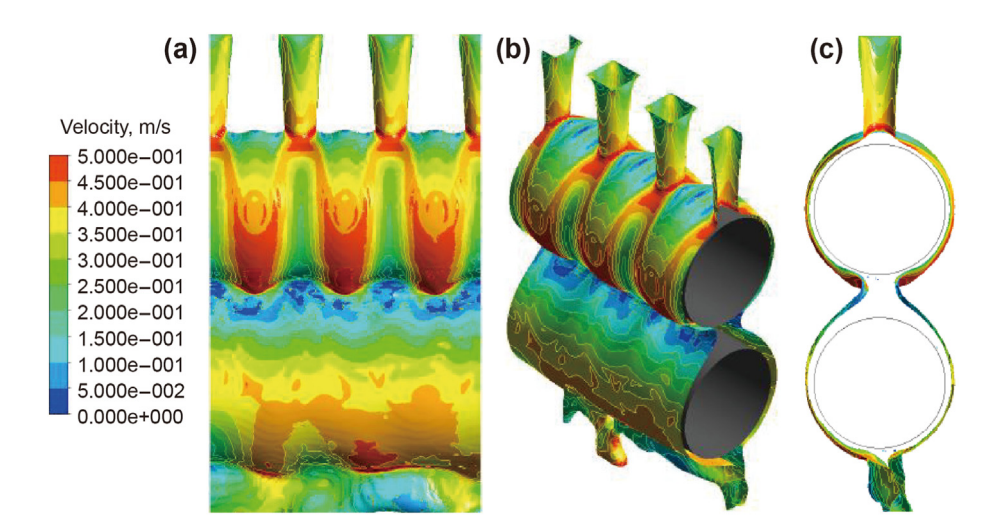


Fig. 11. The falling film flow characteristics and velocity distribution of LH₂ mixed refrigerant with $m_G = 3.6$ kg/h ($\nu_G = 0.508$ m 3 /h), $m_L = 28.8$ kg/h ($\nu_L = 0.034$ m 3 /h).

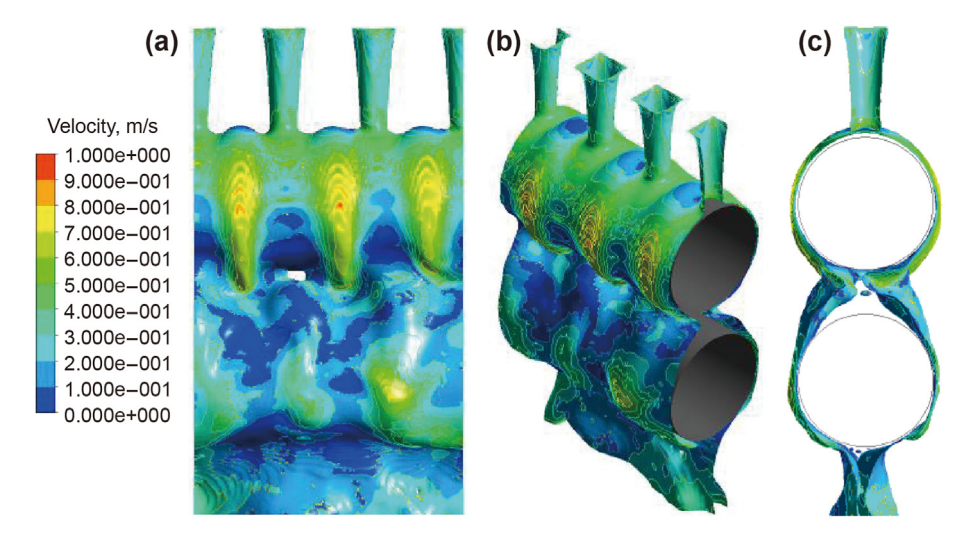


Fig. 12. The wavy film flow characteristics and velocity distribution of LH₂ mixed refrigerant with $m_G = 18$ kg/h ($\nu_G = 2.539$ m³/h), $m_L = 21.6$ kg/h ($\nu_L = 0.025$ m³/h).

current gas flow on the peak area of thicker liquid film in the first tube is stronger, with a decrease in the thickness of upper liquid film and an increase in the thickness of lower liquid film. At 68.889 ms, the gas flow has a relatively small impact on liquid film of the first tube, while rippling and sagging liquid belly gradually appears on liquid film of the second tube. At 84.959 ms, the ripple and

sagging liquid belly of the second tube are more obvious, and the speed is becoming faster. From 124.264 ms to 159.879 ms, both ripple and liquid belly phenomena of liquid film disappear, and liquid film gradually becomes smoother with only a small amount of ripple.

The shear film flow characteristics and velocity distribution with

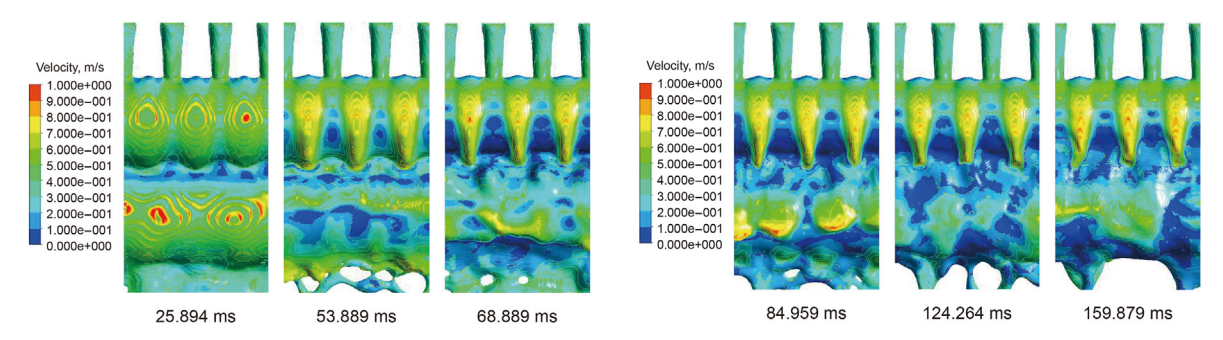


Fig. 13. The wavy film flow characteristics and velocity distribution of LH₂ mixed refrigerant with $m_G = 18$ kg/h ($v_G = 2.539$ m³/h), $m_L = 28.8$ kg/h ($v_L = 0.034$ m³/h).

 $m_G = 36 \text{ kg/h} (v_G = 5.078 \text{ m}^3/\text{h}), m_L = 21.6 \text{ kg/h} (v_L = 0.025 \text{ m}^3/\text{h})$ and 28.8 kg/h ($v_L = 0.034 \text{ m}^3/\text{h}$) are shown in Figs. 14 and 15. The flow pattern of LH₂ mixed refrigerant evolves from wavy film flow pattern to shear film flow pattern. As shown in Fig. 14, at 34.006 ms, a large number of liquid filaments appear. This is because the cocurrent gas flow rate is greater than liquid flow. Liquid film is sheared by the turbulent co-current gas flow and falls from the tube wall. The liquid film gradually begins to break and form layer by layer waves. The flow rate of liquid refrigerant becomes very fast, and liquid film thickness greatly decreases. At 96.512 ms, the liquid film is relatively flat and thin with the shear effect of gas flow. When liquid phase flow rate $m_L = 28.8 \text{ kg/h}$, the flow characteristics and velocity distribution of liquid hydrogen falling film with complex mixed refrigerants over time are shown in Fig. 15. From 53.43 ms to 60.93 ms, the liquid film becomes large droplet or liquid filament. The speed of liquid droplet is faster, resulting in a stronger

shear effect of gas on the liquid film. From 85.93 ms to 120.93 ms, due to the faster droplet velocity, a large amount of liquid rapidly drops, and liquid film of the second tube appears thin and flat. At 158.525 ms, the thick liquid film is sheared to droplets and large waves. At 181.951 ms, the liquid film returns to the state of 83.93 ms and 120.93 ms. At 233.484 ms, large droplets and filaments reappear and fall very quickly, resulting in discontinuous flow patterns between tubes. From 248.859 ms to 251.684 ms, the falling film flow returns to a thin liquid film state due to the shear effect of gas flow.

The mist flow characteristics and velocity distribution with $m_{\rm G}=180$ kg/h ($v_{\rm G}=25.388$ m 3 /h), $m_{\rm L}=21.6$ kg/h ($v_{\rm L}=0.025$ m 3 /h) and 28.8 kg/h ($v_{\rm L}=0.034$ m 3 /h) are shown in Figs. 16 and 17. The gas-phase flow rate of mixed refrigerant is far greater than liquid-phase flow rate. The flow pattern of LH $_2$ mixed refrigerant evolves from shear film flow pattern to mist flow pattern. As shown

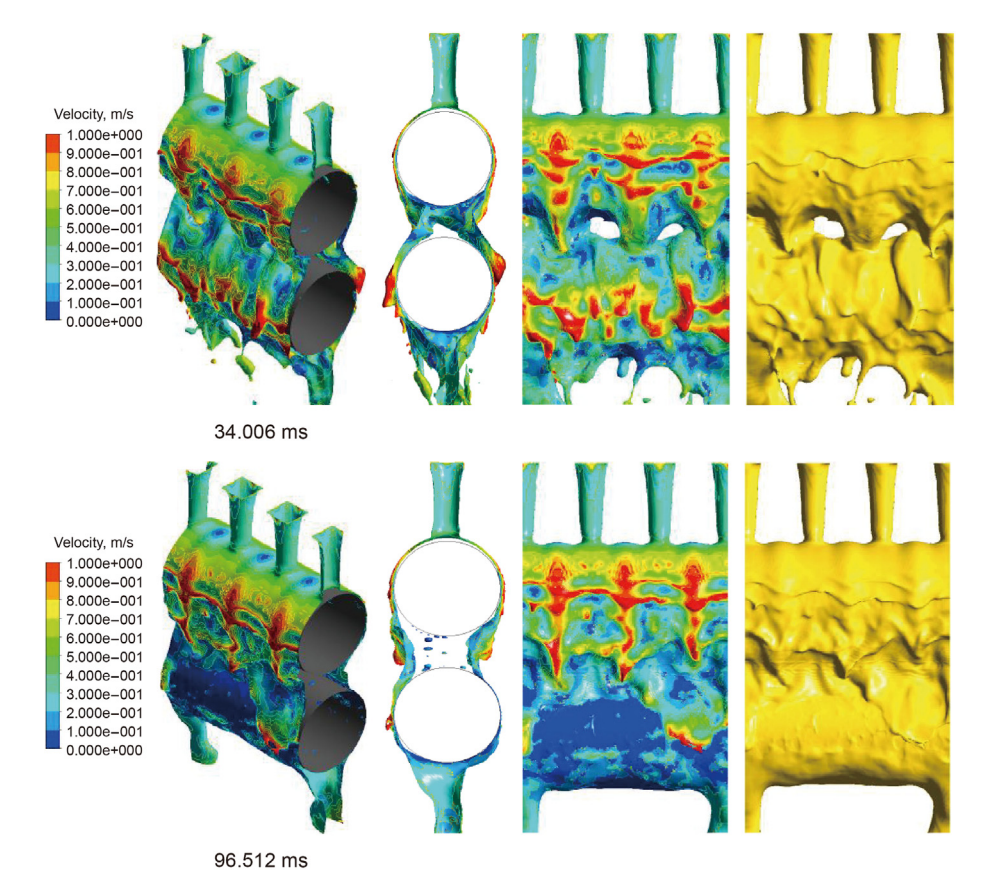


Fig. 14. The shear film flow characteristics and velocity distribution of LH₂ mixed refrigerant with $m_G = 36$ kg/h ($\nu_G = 5.078$ m³/h), $m_L = 21.6$ kg/h ($\nu_L = 0.025$ m³/h).

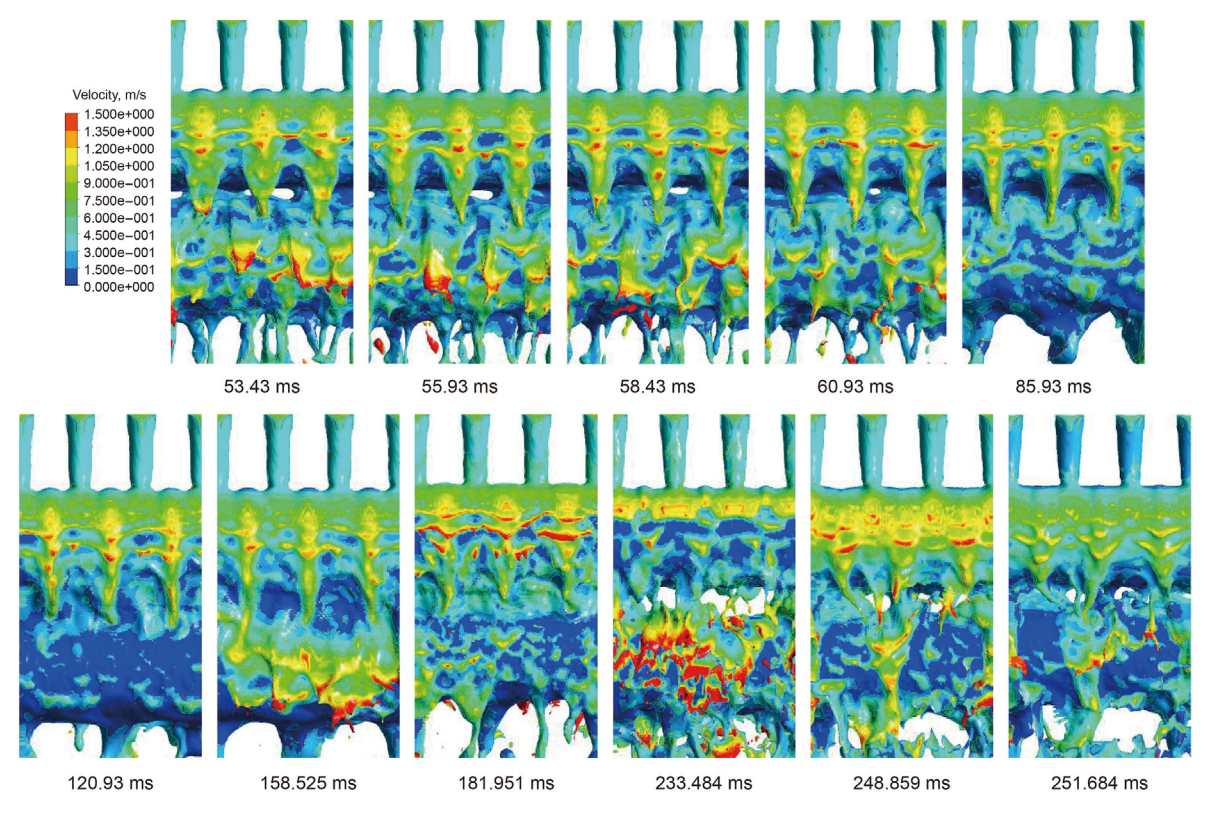
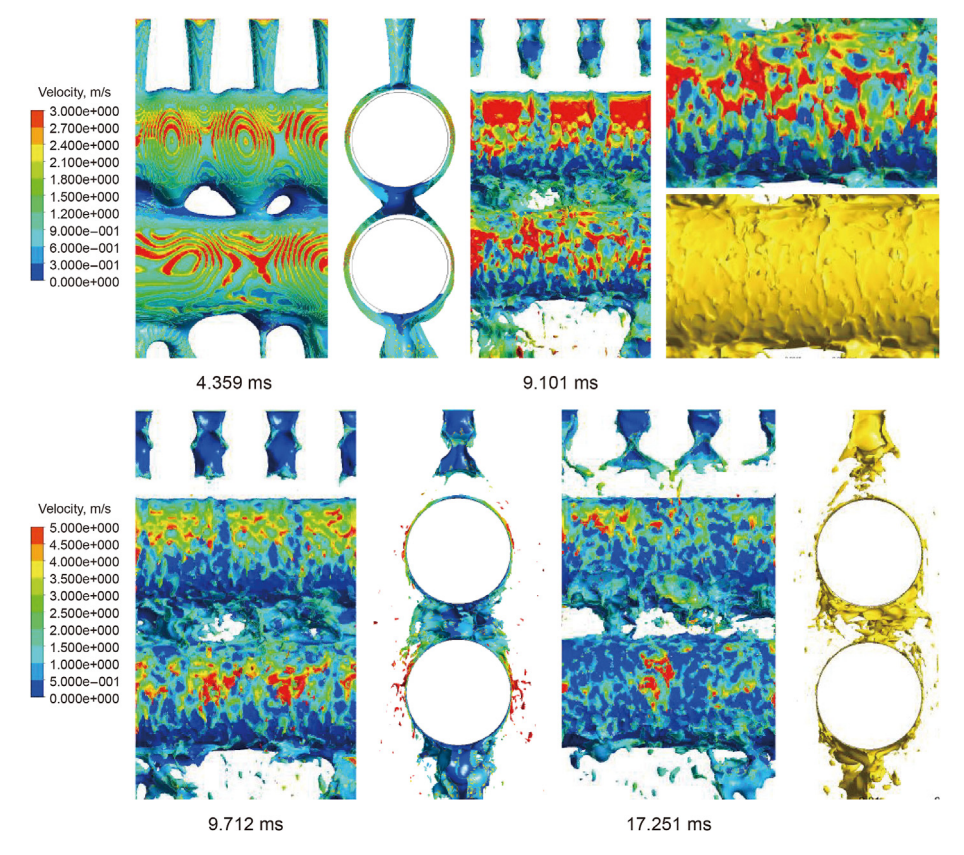


Fig. 15. The shear film flow characteristics and velocity distribution of LH₂ mixed refrigerant with $m_G = 36$ kg/h ($v_G = 5.078$ m 3 /h), $m_L = 28.8$ kg/h ($v_L = 0.034$ m 3 /h).



 $\textbf{Fig. 16.} \ \ \text{The mist flow characteristics and velocity distribution of LH}_2 \ \text{mixed refrigerant with} \ m_G = 180 \ \text{kg/h} \ (\nu_G = 25.388 \ \text{m}^3/\text{h}), \ m_L = 21.6 \ \text{kg/h} \ (\nu_L = 0.025 \ \text{m}^3/\text{h}).$

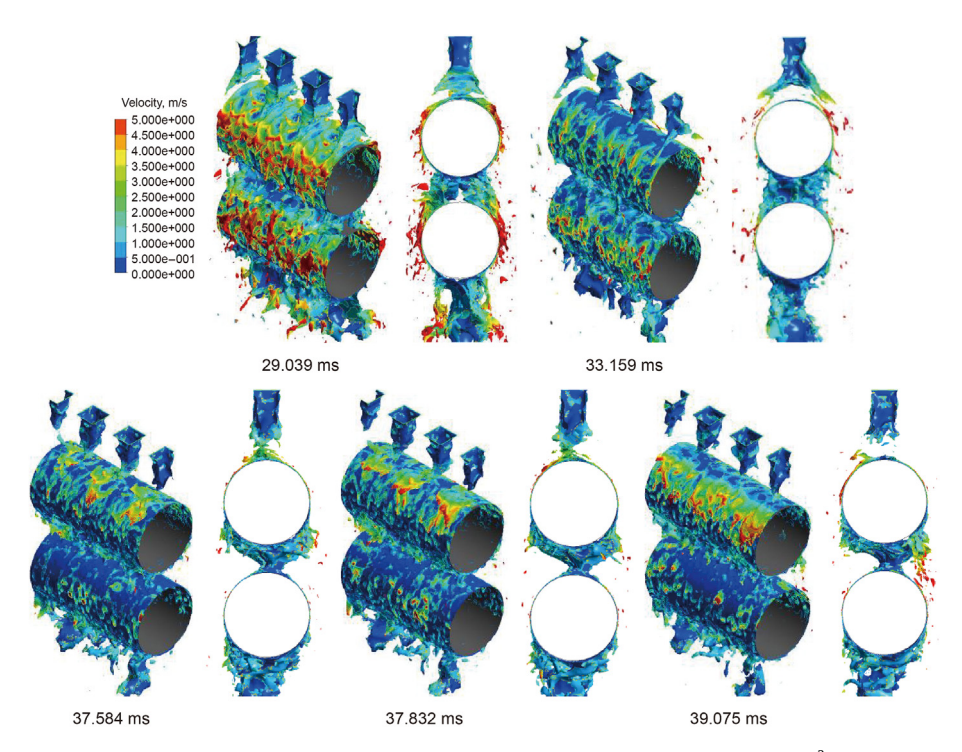


Fig. 17. The mist flow characteristics and velocity distribution of LH₂ mixed refrigerant with $m_G = 180$ kg/h ($v_G = 25.388$ m³/h), $m_L = 28.8$ kg/h ($v_L = 0.034$ m³/h).

in Fig. 16, at 4.359 ms, the falling film flow characteristics have not undergone significant changes. The obvious ripple characteristics appear on the liquid film surface. At 9.101 ms, the gas phase flow rate of mixed refrigerant is much greater than liquid phase flow rate, which has a significant impact on the upper liquid flow rate. The liquid film is sheared and broken into droplets and long liquid filaments. From 9.712 ms to 17.251 ms, the gas flow exerts a strong shear effect on the inlet liquid column, causing the liquid to directly break into mist like droplets at the inlet, and the droplets disperse around the tube. When the liquid phase mass flow rate increases to 28.8 kg/h ($v_L = 0.034 \text{ m}^3/\text{h}$), the flow characteristics and velocity distribution of LH₂ complex mixed refrigerants over time are shown in Fig. 17. At 29.039 ms, the liquid film begins to break into high-speed droplets and filaments with the shear effect of cocurrent gas flow. At 33.159 ms, the liquid column is sheared and destroyed by gas flow. The liquid column disperse to form droplets, and high-speed droplets continue to disperse. From 37.584 ms to 39.075 ms, the liquid column continue to break, and the flow velocity of droplets in the upper part of tube is greater than that in the lower part.

From Figs. 10—17, it can be concluded that with the increase of co-current gas flow, the flow pattern of mixed refrigerant changes from falling film flow pattern (column flow, sheet-column flow, sheet flow), via wavy film flow pattern, and shear film flow pattern, to mist flow pattern.

The film flow thickness distribution with the effect of co-current gas flow is given in Fig. 18. With $m_G=18~{\rm kg/h}$, when circumferential angles are 20° , 40° , 60° , 80° , 100° and 120° , the maximum liquid film thicknesses are 1.17 mm, 1.05 mm, 0.93 mm, 0.87 mm, 1.05 mm and 1.58 mm, and velocities are $0.28~{\rm m/s}$, $0.46~{\rm m/s}$, $0.57~{\rm m/s}$, $0.68~{\rm m/s}$, $0.90~{\rm m/s}$ and $0.73~{\rm m/s}$, respectively. When the circumferential angle is 60° , with $m_G=0~{\rm kg/h}$, $3.6~{\rm kg/h}$, $18~{\rm kg/h}$ and $36~{\rm kg/h}$, the maximum liquid film thicknesses are $0.96~{\rm mm}$, $0.96~{\rm mm}$, $0.93~{\rm mm}$ and $0.63~{\rm mm}$, and velocities are $0.31~{\rm m/s}$, $0.32~{\rm m/s}$, $0.57~{\rm m/s}$ and $1.11~{\rm m/s}$, respectively. When the circumferential angle is 120° , with $m_G=0~{\rm kg/h}$, $3.6~{\rm kg/h}$, $18~{\rm kg/h}$ and

36 kg/h, the maximum liquid film thicknesses are 0.78 mm, 0.88 mm, 1.58 mm and 1.50 mm, and velocities are 0.44 m/s, 0.47 m/s, 0.73 m/s and 0.90 m/s, respectively. When $m_L = 28.8$ kg/h and $m_G = 36$ kg/h, at circumferential angles of 20° , 40° , 80° , 100° , 120° , the average liquid film thickness is 0.7357 mm, 0.4279 mm, 0.3430 mm, 0.4512 mm, 0.7667 mm, respectively. The minimum liquid film thickness is 0.4506 mm, 0.3023 mm, 0.1840 mm, 0.1927 mm, 0.2807 mm, respectively. The results show that liquid film thickness on the upper part of tube decreases and the thickness on the lower part increases due to shear effect of co-current gas flow.

The mechanism of instability and fragmentation of liquid film and flow pattern transition with the effect of co-current gas flow is shown in Fig. 19. From Fig. 19(a), the velocity of gas-phase refrigerant is greater than that of liquid-phase refrigerant. With the influence of fluid viscosity, the interlayer fault can be expanded into a transition layer. Due to large gradient of fluid velocity, shear force becomes the main force in transition layer, and transition layer exhibits the properties of a shear layer. The fluid rotates on the tangential velocity discontinuity, making it a vortex layer. The vortex layer is unstable and can be deformed by small disturbances, ultimately curling into a single vortex. This phenomenon is called Kelvin Helmholtz instability. The velocity difference between gas and liquid with the shear effect of co-current gas flow is one of the important factors causing Kelvin Helmholtz instability waves in the liquid film. During the propagation of waves, the amplitude gradually increases, ultimately leading to the rupture of liquid film. Therefore, the Kelvin Helmholtz instability is the main factor causing the rupture and atomization of liquid film.

Through the investigation, this paper analyzes three typical instability modes of LH₂ mixed refrigerant, including wavy flow pattern (Fig. 19(b), $GLR = m_C/m_L = 0.625$, 0.833), shear flow pattern (Fig. 19(c), GLR = 1.25, 1.667) and mist flow pattern (Fig. 19(d), GLR = 6.25, 8.333), corresponding to the instability and fragmentation process of liquid film.

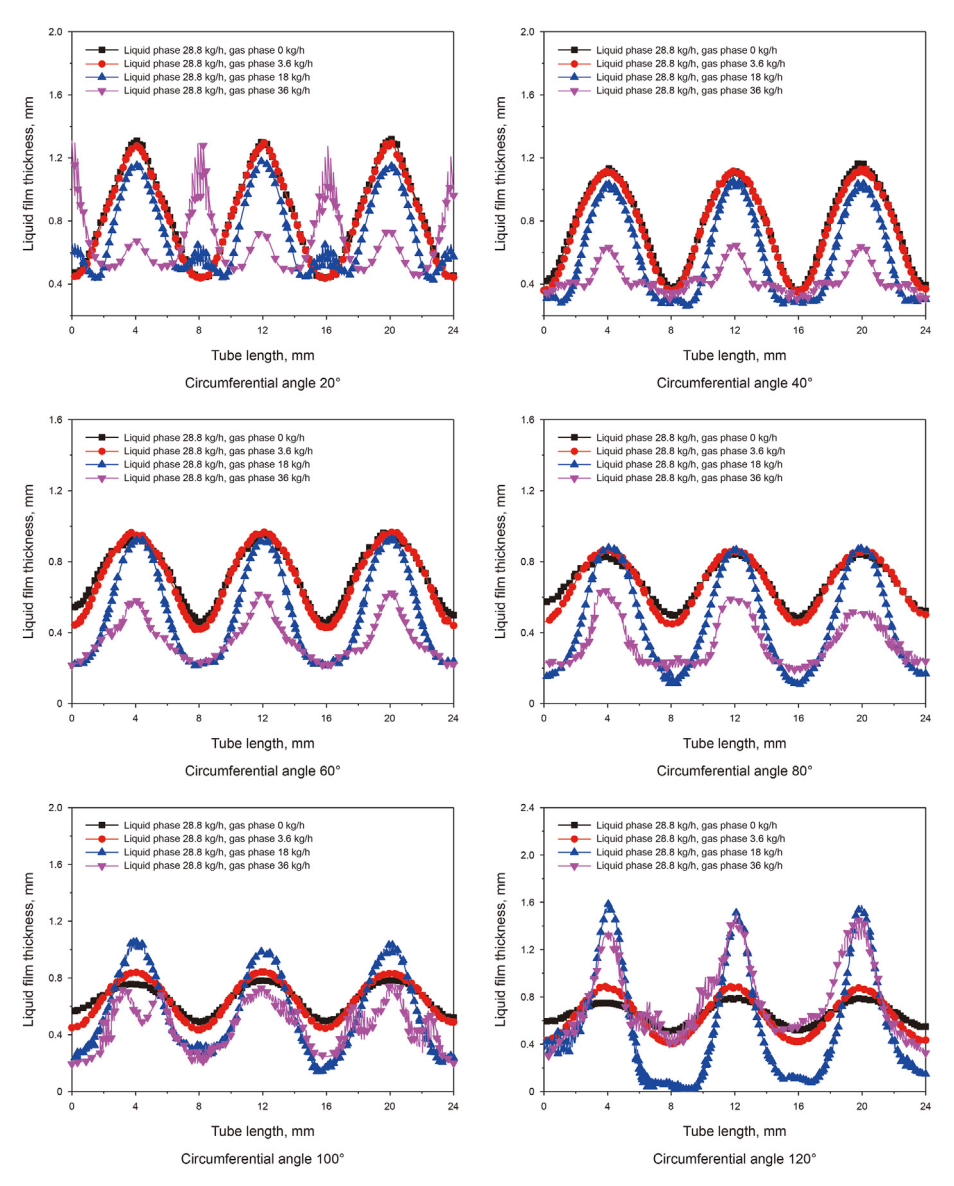


Fig. 18. The film flow thickness distribution with the effect of co-current gas flow.

1. Wave instability of wavy flow pattern

As shown in Fig. 19(b), with the relative motion of liquid and gas, the curvature radius of liquid surface changes, increasing the effect of surface tension. Then the surface static pressure changes. The liquid contracts into a thicker liquid belly at the edge, and the liquid belly becomes unstable with aerodynamic force and surface tension. This type of liquid film instability often occurs when the liquid-phase viscosity and surface tension are both high, and the gas-phase force is not strong. The main factor contributing to instability is the liquid-phase surface tension.

2. Shear instability fragmentation of shear flow pattern

As shown in Fig. 19(c), with a large velocity of gas flow, the gasphase inertial force is the main control force of this mechanism. The surface of liquid film generates disturbance waves, which continuously grow with time and space. When the amplitude of surface wave increases to the thickness of liquid film, the liquid film is torn to form liquid filaments. Under the action of surface tension, the

liquid filaments further break and form droplets, generating non-uniform sized droplets.

3. Foggy fragmentation of mist flow pattern

As shown in Fig. 19(d), when the relative velocity between the liquid-phase and gas-phase medium further increases, the gas-phase inertial force is much greater than the liquid-phase surface tension. The liquid film is strongly disturbed and broken into fine droplets at nozzle outlet.

3.3. Key parameters of cryogenic heat transfer process changing with time

Dynamic responses of key parameters in cryogenic heat transfer process are illustrated in Fig. 20. The falling film heat transfer experiment of cryogenic mixed refrigerant lasting about 30000 s is divided into seven parts. In the cryogenic spiral wound heat exchanger, the feed gas, gas-phase and liquid-phase refrigerant absorb the cooling capacity. After passing through the low-

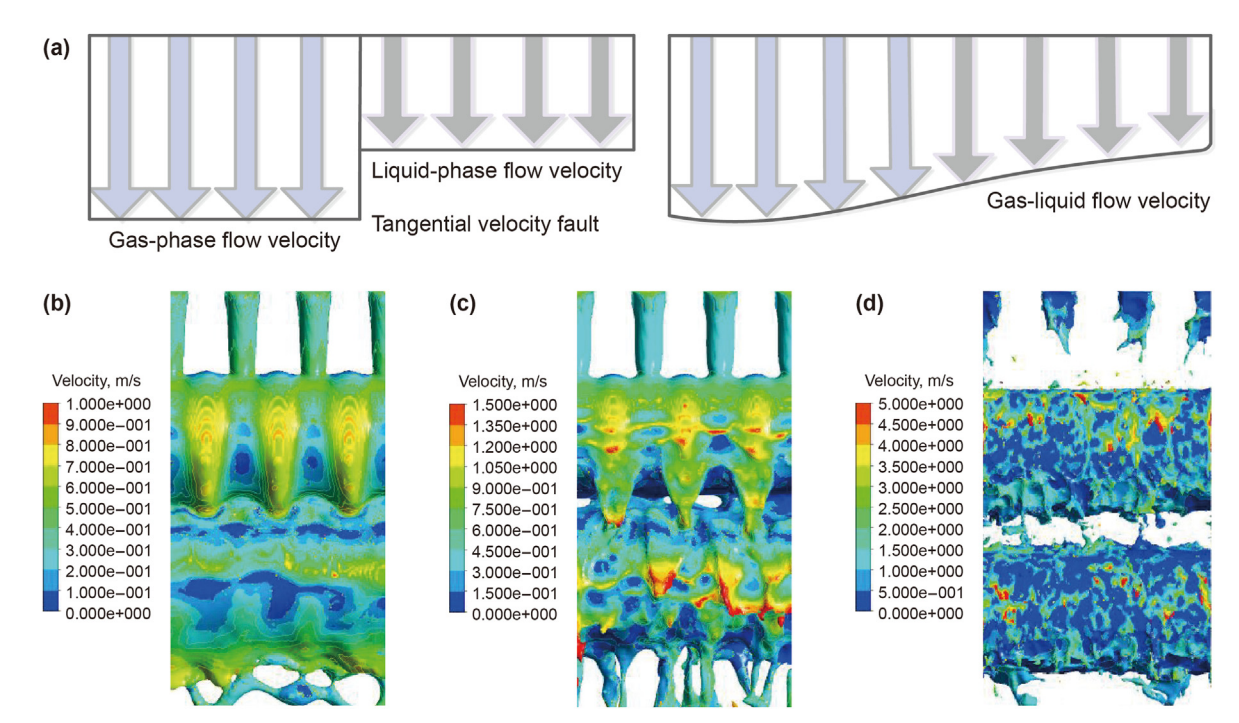


Fig. 19. Mechanism of instability and fragmentation of liquid film and flow pattern transition with the effect of co-current gas flow: (a) Fault between gas-phase flow velocity and liquid-phase flow velocity; (b) wave instability of wavy flow pattern; (c) shear instability fragmentation of shear flow pattern; (d) foggy fragmentation of mist flow pattern.

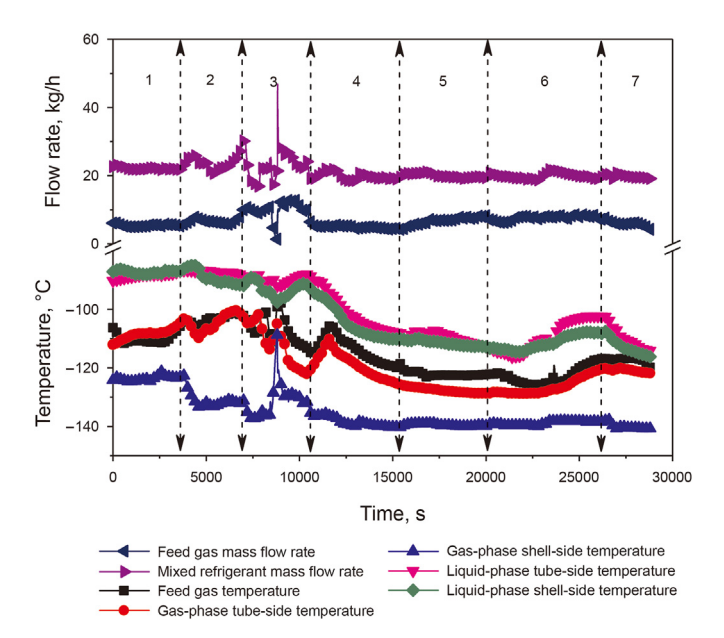


Fig. 20. Key process parameters changing with time: (1) steady region, (2) disturbance region of small fluctuations in feed gas and mixed refrigerant flow rates, (3) disturbance region of large fluctuations in feed gas and mixed refrigerant flow rates,(4) disturbance region of small fluctuations in mixed refrigerant flow rate, (5) disturbance region of increase of feed gas flow rate, (6) disturbance region of small fluctuations in mixed refrigerant flow rate, (7) disturbance region of decrease of feed gas flow rate.

temperature throttle valve for cooling and pressure reduction, the tube-side gas-phase and liquid-phase refrigerant becomes the shell-side refrigerant. Shell-side refrigerant flows from top to bottom in cryogenic spiral wound heat exchanger, which provides the cooling capacity to feed gas.

At the initial stage of cryogenic heat transfer experiment, the

mass flow rates and temperatures maintain stable. In the second stage, the mass flow rates of feed gas and mixed refrigerant increase slightly at 3700 s. Then the mixed refrigerant flow rises again after fluctuation. The temperatures of feed gas and liquid-phase mixed refrigerant basically remain stable, while the temperature of gas-phase mixed refrigerant changes more sharply. At 7000 s, the flow rates of mixed refrigerant and feed gas fluctuate sharply, resulting in the temperature fluctuation. In the fourth stage, the feed gas flow maintains stable, and refrigerant flow fluctuates slightly. Because of the hysteresis of temperature, the mass flow in previous stage changes greatly, and the temperature changes sharply in this stage. In the fifth stage, the feed gas flow increases slightly, which suppresses the trend of temperature decline. The temperature is rising in the sixth stage, reflecting the hysteresis of temperature change. The small increase of mixed refrigerant flow has not restrained the rising trend of temperature. Finally, the liquid-phase tube-side and shell-side temperatures decrease sharply due to the decrease of feed gas flow rate. This is because the decrease in the flow rate of feed gas results in a higher cooling capacity of the refrigerant. In the cryogenic spiral wound heat exchanger, the cooling capacity absorption of gas-phase refrigerant and feed gas is divided into sensible heat and liquefaction latent heat, while the liquid-phase refrigerant only has sensible heat. Therefore, an increase in the cooling capacity of the refrigerant has a greater impact on the liquid-phase refrigerant. It can be concluded that in cryogenic heat transfer process of falling film evaporation, the temperatures are much more sensitive to mass flow rates.

4. Conclusions

A cryogenic experimental device, visualization experimental device and three-dimensional (3D) numerical simulation of falling film flow with the effect of co-current gas flow in LH₂ unit are constructed to study heat transfer temperatures, falling film flow

pattern, liquid film distribution of SWHE, based on the high-speed camera and cryogenic refrigeration cycle, the coupled VOF and Level Set two-phase flow model. Following conclusions can be drawn.

- 1. The liquid film of LH₂ mixed refrigerant with column flow pattern can not uniformly and completely cover the tube wall surface ($m_{\rm L}=7.2$ kg/h, 10.8 kg/h, 14.4 kg/h). When the circumferential angle is around 140°, the drying area of the liquid film is the largest. With the increase of liquid-phase mass flow rates ($m_{\rm L}=21.6$ kg/h, 28.8 kg/h), the falling film flow pattern evolves into sheet-column flow and sheet flow, and the liquid film completely covers the tube wall surface.
- 2. The liquid film thickness distribution of mixed refrigerant is more regular when the circumferential angle is small. With the increase of circumferential angle, the stability of liquid film between the wave peaks becomes worse. At the same circumferential position, the flow rate has a great influence on the liquid film thickness distribution. With sheet-column flow pattern, the distribution regularity of liquid film is poor, and the fluctuation of liquid film at the same circumference is large. When the flow pattern is complete sheet flow, the uniformity of liquid film becomes better.
- 3. With the increase of co-current gas flow of LH₂ mixed refrigerant, the liquid film gradually becomes unstable. The flow pattern of mixed refrigerant changes from falling film flow pattern (column flow, sheet-column flow, sheet flow), via wavy film flow pattern ($GLR = m_C/m_L = 0.625, 0.833$), and shear film flow pattern (GLR = 1.25, 1.667), to mist flow pattern (GLR = 6.25, 8.333). There are three typical instability modes of liquid film, including wave instability of wavy film flow pattern, shear instability and fragmentation of shear film flow pattern, and foggy fragmentation of mist flow pattern. Due to the shear effect of co-current gas flow, the liquid film thickness on the upper part of tube decreases, and the thickness on the lower part increases.
- 4. The flow rates of gas-phase and liquid-phase mixed refrigerant have a great influence on the liquid film spreading process, falling film flow pattern and heat transfer performance. In the process of falling film heat transfer of low temperature mixed refrigerant, the small fluctuation of flow rates of feed gas and mixed refrigerant can greatly affect the heat transfer characteristics of spiral wound heat exchanger.

CRediT authorship contribution statement

Chong-Zheng Sun: Conceptualization, Data curation, Formal analysis, Software, Visualization, Writing — original draft. **Yu-Xing Li:** Methodology, Validation, Writing — review & editing. **Hui Han:** Resources, Software. **Xiao-Yi Geng:** Investigation. **Xiao Lu:** Conceptualization, Methodology, Project administration, Writing — review & editing.

Declaration of competing interest

We declare that we have no financial and personal relationships with other people or organizations that can inappropriately influence the manuscript entitled "Numerical and experimental study on the falling film flow characteristics with the effect of co-current gas flow in hydrogen liquefaction process".

Acknowledgements

The present work is supported by the National Natural Science

Foundation of China (52304067, 62273213), the Natural Science Foundation of Shandong Province of China (ZR2021QE073), the Natural Science Foundation of Shandong Province for Innovation and Development Joint Funds (ZR2022LZH001), the China Postdoctoral Science Foundation (2023M732111).

References

- Ansarinasab, H., Mehrpooya, M., Sadeghzadeh, M., 2019. An exergy-based investigation on hydrogen liquefaction plant-exergy, exergoeconomic, and exergoenvironmental analyses. J. Clean. Prod. 210, 530–541. https://doi.org/10.1016/j.jclepro.2018.11.090.
- Asadnia, M., Mehrpooya, M., 2017. A novel hydrogen liquefaction process configuration with combined mixed refrigerant systems. Int. J. Hydrogen Energy 2 (23), 15564–15585. https://doi.org/10.1016/j.ijhydene.2017.04.260.
- Bohra, L.K., Lee, S., Garimella, S., 2019. Visual documentation of transfer processes in horizontal-tube falling-film ammonia—water absorbers. Int. J. Refrig. 103, 91–105. https://doi.org/10.1016/j.ijrefrig.2019.03.032.
- Brackbill, J.U., Kothe, D.B., Zemach, C., 1992. A continuum method for modeling surface tension. J. Comput. Phys. 100 (2), 335–354. https://doi.org/10.1016/ 0021-9991(92)90240-Y.
- Chen, J.D., Zhang, R.H., Niu, R.P., 2015. Numerical simulation of horizontal tube bundle falling film flow pattern transformation. Renew. Energy 73, 62–68. https://doi.org/10.1016/j.renene.2014.08.007.
- Chen, X., Liu, X.H., Shen, S.Q., et al., 2015. Experimental study on heat transfer of falling film evaporation outside horizontal tube. J. Sol. Energy 8, 1996–2001.
- Chen, X., Wang, J., Lu, T., et al., 2022. Three-dimensional film thickness distribution of horizontal tube falling film with droplet and sheet flow. Int. J. Multiphas. Flow 148, 103933. https://doi.org/10.1016/j.ijmultiphaseflow.2021.103933.
- Chung, H., Wusiman, K., Kim, S., et al., 2012. Liquid film falling behaviour on horizontal circular cylinder. J. Cent. S. Univ. 19, 1353—1358.
- Ding, S.J., Peng, S.Z., Yan, Z.J., et al., 2022. Charge effects on quinoline hydro-denitrogenation catalyzed by Ni-Mo-S active sites-A theoretical study by DFT calculation. Petrol. Sci. 19 (1), 339–344. https://doi.org/10.1016/i.petsci.2021.10.021.
- Ebrahimi, A., Ghorbani, B., Ziabasharhagh, M., 2020. Pinch and sensitivity analyses of hydrogen liquefaction process in a hybridized system of biomass gasification plant, and cryogenic air separation cycle. J. Clean. Prod. 258, 120548. https:// doi.org/10.1016/j.jclepro.2020.120548.
- Eskin, D., 2022. An engineering model of heat transfer through a turbulent falling film for a condensing vapor flow. Chem. Eng. Res. Des. 187, 1–8. https://doi.org/10.1016/j.cherd.2022.08.047.
- Guo, R., Bai, X., Lu, Y., et al., 2022. Hydrogen solubility prediction for diesel molecules based on a modified Henry equation. Petrol. Sci. 19 (1), 363–374. https://doi.org/10.1016/j.petsci.2021.10.020.
- Havestini, R.A., Ormiston, S.J., 2022. Detailed two-phase numerical analysis of falling film absorption over a horizontal tube. Int. J. Heat Mass Tran. 198, 123378. https://doi.org/10.1016/j.ijheatmasstransfer.2022.123378.
- He, M.G., Wang, X.F., Zhang, Y., 2007. Study on liquid flow outside the horizontal tube falling film evaporator and Simulation of film thickness. Therm. Sci. Technol. 6 (4), 319–325.
- Hou, H., Bi, Q., Ma, H., et al., 2012. Distribution characteristics of falling film thickness around a horizontal tube. Desalination 285, 393–398. https://doi.org/ 10.1016/j.desal.2011.10.020.
- Kofman, N., Mergui, S., Ruyer-Quil, C., 2017. Characteristics of solitary waves on a falling liquid film sheared by a turbulent counter-current gas flow. Int. J. Multiphas. Flow 95, 22–34. https://doi.org/10.1016/j.ijmultiphaseflow.2017.05.007.
- Krasae-in, S., Bredesen, A.M., Stang, J.H., et al., 2011. Simulation and experiment of a hydrogen liquefaction test rig using a multi-component refrigerant refrigeration system. Int. J. Hydrogen Energy 36 (1), 907–919. https://doi.org/10.1016/ iiihydene 2010 09 005
- Li, M., Lu, Y., Zhang, S., et al., 2016. A numerical study of effects of counter-current gas flow rate on local hydrodynamic characteristics of falling films over horizontal tubes. Desalination 383, 68–80. https://doi.org/10.1016/j.idesal.2016.01.016.
- Li, Y.L., Wang, K., Wu, W., et al., 2017. Study on the effect of refrigerant distributing nonuniformity on the performance of falling-film evaporator with liquid recirculation system. Int. J. Refrig. 82, 199–211. https://doi.org/10.1016/j.ijrefrig.2017.05.032.
- Lin, S., Liu, X., Li, X., 2019. The spatial distribution of liquid film thickness outside the horizontal falling film tube. Int. J. Heat Mass Tran. 143, 118577. https:// doi.org/10.1016/j.ijheatmasstransfer.2019.118577.
- Liu, S., Shen, S., Mu, X., et al., 2019. Experimental study on droplet flow of falling film between horizontal tubes. Int. J. Multiphas. Flow 118, 10–22. https:// doi.org/10.1016/j.ijmultiphaseflow.2019.05.008.
- Mitrovic, J., 2005. Flow structures of a liquid film falling on horizontal tubes. Chem. Eng. Technol. 28 (6), 684–694. https://doi.org/10.1002/ceat.200500064.
- Nusselt, W., 1916. Die oberflachenkondensation des wasserdampfes. VDI-Z (Ver. Dtsch. Ingenieure-Z) 60, 569–575 (In German).
- Qi, R., Dong, C., Yu, S., et al., 2021. Modelling and experiments of falling film breakup characteristics considering mass transfer for liquid desiccant dehumidification. Int. J. Heat Mass Tran. 181, 122027. https://doi.org/10.1016/

- j.ijheatmasstransfer.2021.122027.
- Sadaghiani, M.S., Mehrpooya, M., 2017. Introducing and energy analysis of a novel cryogenic hydrogen liquefaction process configuration. Int. J. Hydrogen Energy 42 (9), 6033–6050. https://doi.org/10.1016/j.ijhydene.2017.01.136.
- Shen, S., Chen, X., Mu, X., et al., 2015. Heat transfer characteristics of horizontal tube falling film evaporation for desalination. Desalination Water Treat. 55 (12), 3343–3349. https://doi.org/10.1080/19443994.2014.946726.
- Skaugen, G., Berstad, D., Wilhelmsen, Ø., 2020. Comparing exergy losses and evaluating the potential of catalyst-filled plate-fin and spiral-wound heat exchangers in a large-scale Claude hydrogen liquefaction process. Int. J. Hydrogen Energy 45 (11), 6663–6679. https://doi.org/10.1016/j.iihydene.2019.12.076.
- Son, H., Yu, T., Hwang, J., et al., 2022. Simulation methodology for hydrogen liquefaction process design considering hydrogen characteristics. Int. J. Hydrogen Energy 47 (61), 25662–25678. https://doi.org/10.1016/j.ijhydene.2022.05.293.
- Sun, C.Z., Cao, X.W., Li, Y.X., et al., 2021. Improvement of offshore adaptability of main cryogenic heat exchanger in FLNG dual mixed refrigerant liquefaction process. Int. J. Heat Mass Tran. 169, 120909. https://doi.org/10.1016/ i.iiheatmasstransfer.2021.120909.
- Sun, H., Geng, J., Wang, C., et al., 2022. Optimization of a hydrogen liquefaction process utilizing mixed refrigeration considering stages of ortho-para hydrogen conversion. Int. J. Hydrogen Energy 47 (39), 17271–17284. https://doi.org/ 10.1016/j.ijhydene.2022.03.215.
- Sun, C.Z., Liu, L., Li, Y.X., et al., 2022a. Research on the falling film flow and heat transfer characteristics of FLNG spiral wound heat exchanger under sea conditions. Petrol. Sci. 19 (3), 1276–1290. https://doi.org/10.1016/j.petsci.2021.12.026.
- Sun, C.Z., Fan, X., Li, Y.X., et al., 2022b. Research on the offshore adaptability of new offshore ammonia-hydrogen coupling storage and transportation technology. Renew. Energy 201, 700—711. https://doi.org/10.1016/i.renene.2022.11.017.
- Sun, H., Huang, W., Zhao, C., et al., 2023. Experimental and numerical study on the falling film flow process on the outer wall of dome cylinder. Int. J. Heat Mass Tran. 216, 124542. https://doi.org/10.1016/j.ijheatmasstransfer.2023.124542.
- Sussman, M., Puckett, E.G., 2000. A coupled level set and volume-of-fluid method

- for computing 3d and axisymmetric incompressible two-phase flows. J. Comput. Phys. 162 (2). https://doi.org/10.1006/jcph.2000.6537, 301-33.
- Teng, L., Li, X.G., Shan, Z.W., et al., 2023. Numerical study of inhibition mechanism of high-pressure hydrogen leakage self-ignition with the addition of ammonia. Petrol. Sci. https://doi.org/10.1016/j.petsci.2023.03.025.
- Wang, X.F., Jacobi, A.M., 2014. A thermodynamic basis for predicting falling-film mode transitions. Int. J. Refrig. 43, 123–132. https://doi.org/10.1016/j.ijrefrig.2014.04.002.
- Wang, X.F., He, M.G., Zhang, Y., 2008. Numerical simulation of liquid flow outside the horizontal tube falling film evaporator, J. Eng. Thermophys. 29 (8), 117–122.
- Wang, J., Chen, X., Lu, T., et al., 2019. Three-dimensional film thickness distribution of horizontal tube falling film with column flow. Appl. Therm. Eng. 154, 140–149. https://doi.org/10.1016/j.applthermaleng.2019.03.041.
- Xie, F., Xia, S., Zhu, Y., et al., 2022. Experimental study on small-scale hydrogen liquefaction of 0.5 L/h. Int. J. Hydrogen Energy 47 (90), 38258—38270. https://doi.org/10.1016/j.ijhydene.2022.08.304.
- Xu, P., Wen, J., Wang, S., et al., 2022a. Study on performance comparison of different fin combinations of catalyst filled plate fin heat exchanger for hydrogen liquefaction. Int. J. Hydrogen Energy 47 (56), 23661–23678. https://doi.org/ 10.1016/j.ijhydene.2022.05.157.
- Xu, P., Wen, J., Huang, W., et al., 2022b. Performance study on plain fin filled with catalyst in a plate fin heat exchanger for hydrogen liquefaction. Int. J. Hydrogen Energy 47 (92), 39146–39162. https://doi.org/10.1016/j.ijhydene.2022.09.085.
- Yu, S., Dong, C., Qi, R., 2023. Numerical and experimental research on thickness fluctuation and Marangoni effect of falling film heat&mass transfer: a comprehensive review. Chem. Eng. Sci. 273, 118616. https://doi.org/10.1016/ ices.2023.118616.
- Zhang, Y., He, F., Zhang, G., et al., 2022. Visualization experiment and numerical simulation on behaviors of gas-liquid falling film flow on the air-side of two-row plain finned-tube heat exchanger. Int. J. Heat Mass Tran. 198, 123416. https://doi.org/10.1016/j.ijheatmasstransfer.2022.123416.
- Zhou, M., Tao, P., Di, X., et al., 2023. Numerical study on the effect of co-current gas flow on the falling film flow characteristics outside the horizontal tube. Nucl. Eng. Des. 413, 112510. https://doi.org/10.1016/j.nucengdes.2023.112510.